Pergamon

Int. J. Solids Structures Vol. 32, No. 14, pp. 1963–1978, 1995

0020–7683/95 $9.50 + .00

0020–7683(94)00247–9

SINGLE HARDENING CONSTITUTIVE MODEL FOR SOIL, ROCK AND CONCRETE

POUL V. LADE

Department of Civil Engineering, The Johns Hopkins University, Baltimore, Maryland 21218-2686, U.S.A.

and

MOON K. KIM

Department of Civil Engineering, Yonsei University, Seoul 120-747, Korea

(*Received* 11 *April* 1994; *in revised form* 27 *September* 1994)

Abstract—A constitutive model with a single yield surface has been developed for the behavior of frictional materials such as clay, sand, concrete, and rock. The model is based on concepts of elasticity and plasticity theories. In addition to Hooke's law for the elastic behavior, the framework for the plastic behavior consists of a failure criterion, a nonassociated flow rule, a single yield criterion that describes contours of equal plastic work, and a work-hardening/softening law. The functions that describe these components are all expressed in terms of stress invariants. The model incorporates twelve parameters for frictional materials with effective cohesion such as concrete and rock. These parameters can all be determined from simple experiments such as isotropic compression and triaxial compression tests. Examples of predictions of the behavior of sand in undrained triaxial compression and of concrete under three-dimensional loading conditions are presented.

1. INTRODUCTION

A constitutive model has been developed on the basis of a thorough review and evaluation of data from experiments on frictional materials such as sand, clay, concrete, and rock (Kim and Lade, 1988; Lade and Kim, 1988a,b). The framework for the evaluation and subsequent development consisted of concepts contained in elasticity and work-hardening plasticity theories.

The new model employs a single, isotropic yield surface shaped as an asymmetric teardrop with the pointed apex at the origin of the principal stress space. This yield surface, expressed in terms of stress invariants, describes the locus at which the total plastic work is constant. The total plastic work (due to shear strains as well as volumetric strains) serves as the hardening parameter, and is used to define the location and shape of the yield surfaces. The use of contours of constant plastic work (or any other measure of hardening) as yield surfaces results in mathematical consistency in the model, because the measure of yielding and the measure of hardening are uniquely related through one monotonic function. In addition, application of a single yield surface produces computational efficiency when used in large computer programs. The nonassociated flow rule is derived from a potential function which describes a three-dimensional surface shaped as a cigar with an asymmetric cross-section.

The model is devised such that the transition from hardening to softening occurs abruptly at the peak failure point. Thus, the transition does not involve any points at which the hardening modulus is zero, but the pointed peak is hardly noticeable in actual comparisons with experimental data.

The main principles of the model and the governing equations for each component are reviewed below. Values of material parameters are then determined from drained tests on loose and dense sand, and predictions are made of stress–strain and pore pressure behavior in undrained tests on the loose and dense sand over a range of confining pressures. Material parameters are also determined from tests on plain concrete performed by Kupfer *et al.*

(1969), and predictions of three-dimensional behavior are compared with experimental data for this concrete.

2. SINGLE HARDENING STRESS–STRAIN MODEL

The total strain increments observed in a material when loaded are divided into elastic and plastic components such that

$$d\varepsilon_{ij} = d\varepsilon_{ij}^{e} + d\varepsilon_{ij}^{p}. \tag{1}$$

These strains are then calculated separately, the elastic strains by Hooke's law, and the plastic strains by a plastic stress–strain law. Both are expressed in terms of effective stresses.

Below is a brief review of the framework and the components of the constitutive model. In order that the presentation follows a logic developmental sequence, the components are presented in the following order: elastic behavior, failure criterion, flow rule, yield criterion, and work-hardening/softening law.

2.1. *Elastic behavior*

The elastic strain increments, which are recoverable upon unloading, are calculated from Hooke's law, using a recently developed model for the nonlinear variation of Young's modulus with stress state (Lade and Nelson, 1987). The value of Poisson's ratio, being limited between zero and one half for most materials, is assumed to be constant. The expression for Young's modulus was derived from theoretical considerations based on the principle of conservation of energy. According to this derivation, Young's modulus, E, can be expressed in terms of a power law involving nondimensional material constants and stress functions as follows:

$$E = Mp_a\left[\left(\frac{I_1}{p_a}\right)^2 + R\frac{J_2'}{p_a^2}\right]^{\lambda}, \tag{2}$$

in which

$$R = 6\frac{1+\nu}{1-2\nu} \tag{3}$$

and I_1 is the first invariant of the stress tensor, and J_2' the second invariant of the deviatoric stress tensor, given as follows:

$$I_1 = \sigma_x + \sigma_y + \sigma_z, \tag{4}$$

$$J_2' = \tfrac{1}{6}[(\sigma_x-\sigma_y)^2 + (\sigma_y-\sigma_z)^2 + (\sigma_z-\sigma_x)^2] + \tau_{xy}^2 + \tau_{yz}^2 + \tau_{zx}^2. \tag{5}$$

The parameter p_a is atmospheric pressure expressed in the same units as E, I_1, and $\sqrt{J_2'}$, and the modulus number M and the exponent λ are constant, dimensionless numbers. The three material parameters ν, M, and λ may be obtained from simple tests such as triaxial compression tests, and the model can be used for materials with effective cohesion.

2.2. *Failure criterion*

A general, three-dimensional failure criterion has been developed for soils, concrete, and rock (Lade, 1977, 1982, 1984, 1993a; Kim and Lade, 1984). The criterion is expressed in terms of the first and third stress invariants of the stress tensor:

$$\left[\frac{I_1^3}{I_3}-27\right]\left[\frac{I_1}{p_a}\right]^m=\eta_1, \tag{6}$$

in which I_1 is given by eqn (4) and

$$I_3=\sigma_x\sigma_y\sigma_z+\tau_{xy}\tau_{yz}\tau_{zx}+\tau_{yx}\tau_{zy}\tau_{xz}-(\sigma_x\tau_{yz}\tau_{zy}+\sigma_y\tau_{zx}\tau_{xz}+\sigma_z\tau_{xy}\tau_{yx}). \tag{7}$$

The parameters η_1 and m are constant dimensionless numbers.

In principal stress space, the failure criterion is shaped like an asymmetric bullet with the pointed apex at the origin of the stress axes, and the cross-sectional shape in the octahedral plane is triangular with smoothly rounded edges in a fashion that conforms to experimental evidence.

In order to include the effective cohesion and the tension which can be sustained by concrete and rock, a translation of the principal stress space along the hydrostatic axis is performed. Thus, a constant stress, ap_a, is added to the normal stresses before substitution in eqn (6):

$$\bar{\sigma}_{ij}=\sigma_{ij}+\delta_{ij}ap_a \tag{8}$$

in which 'a' is a dimensionless parameter, and δ_{ij} is Kronecker's delta. The value of ap_a reflects the effect of the tensile strength of the material. The three material parameters, η_1, m, and a, may be determined from the results of simple tests such as triaxial compression tests.

2.3. *Flow rule*

The plastic strain increments are calculated from the flow rule

$$\mathrm{d}\varepsilon_{ij}^p=\mathrm{d}\lambda_p\cdot\frac{\partial g_p}{\partial\sigma_{ij}}, \tag{9}$$

in which g_p is a plastic potential function and $\mathrm{d}\lambda_p$ is a scalar factor of proportionality. A suitable plastic potential function for frictional materials was developed and presented by Kim and Lade (1988). This function is different from the yield function and nonassociated flow is consequently obtained. The plastic potential function is written in terms of the three invariants of the stress tensor:

$$g_p=\left[\psi_1\frac{I_1^3}{I_3}-\frac{I_1^2}{I_2}+\psi_2\right]\left[\frac{I_1}{p_a}\right]^\mu, \tag{10}$$

in which I_1 and I_3 are given by eqns (4) and (7) and the second stress invariant is defined as

$$I_2=\tau_{xy}\tau_{yx}+\tau_{yz}\tau_{zy}+\tau_{zx}\tau_{xz}-(\sigma_x\sigma_y+\sigma_y\sigma_z+\sigma_z\sigma_x). \tag{11}$$

The material parameters ψ_2 and μ are dimensionless constants that may be determined from triaxial compression tests. The parameter ψ_1 is related to the curvature parameter m of the failure criterion as follows:

$$\psi_1=0.00155\times m^{-1.27}. \tag{12}$$

The parameter ψ_1 acts as a weighting factor between the triangular shape (from the I_3 term) and the circular shape (from the I_2 term). The parameter ψ_2 controls the intersection with the hydrostatic axis, and the exponent μ determines the curvature of meridians. The

corresponding plastic potential surfaces are shown in Fig. 1. They are shaped as asymmetric cigars with smoothly rounded triangular cross-sections similar but not identical to those for the failure surfaces.

The derivatives of g_p with regard to the stresses are

$$\frac{\partial g_p}{\partial \sigma_{ij}} = \left[\frac{I_1}{p_a}\right]^{\mu} \begin{Bmatrix} G-(\sigma_y+\sigma_z)\dfrac{I_1^2}{I_2^2}-\psi_1(\sigma_y\sigma_z-\tau_{yz}^2)\dfrac{I_1^3}{I_3^2} \\ G-(\sigma_z+\sigma_x)\dfrac{I_1^2}{I_2^2}-\psi_1(\sigma_z\sigma_x-\tau_{zx}^2)\dfrac{I_1^3}{I_3^2} \\ G-(\sigma_x+\sigma_y)\dfrac{I_1^2}{I_2^2}-\psi_1(\sigma_x\sigma_y-\tau_{xy}^2)\dfrac{I_1^3}{I_3^2} \\ 2\dfrac{I_1^2}{I_2^2}\tau_{yz}-2\psi_1(\tau_{xy}\tau_{zx}-\sigma_x\tau_{yz})\dfrac{I_1^3}{I_3^2} \\ 2\dfrac{I_1^2}{I_2^2}\tau_{zx}-2\psi_1(\tau_{xy}\tau_{yz}-\sigma_y\tau_{zx})\dfrac{I_1^3}{I_3^2} \\ 2\dfrac{I_1^2}{I_2^2}\tau_{xy}-2\psi_1(\tau_{yz}\tau_{zx}-\sigma_z\tau_{xy})\dfrac{I_1^3}{I_3^2} \end{Bmatrix}, \tag{13a–f}$$

where

$$G = \psi_1(\mu+3)\frac{I_1^2}{I_3}-(\mu+2)\frac{I_1}{I_2}+\frac{\mu}{I_1}\psi_2. \tag{14}$$

These derivatives are used to obtain the plastic strain increment from eqn (9).

Once the parameter ψ_1 is evaluated, the other parameters, ψ_2 and μ, can be determined using triaxial compression test data. To do this, the incremental plastic strain ratio is first defined as

$$\nu_p = -\frac{d\varepsilon_3^p}{d\varepsilon_1^p} \tag{15}$$

in which $d\varepsilon_1^p$ and $d\varepsilon_3^p$ are the major and minor plastic strain increments obtained for an axial stress increment in a triaxial compression test. Substitution of eqns (9) and (13) for the

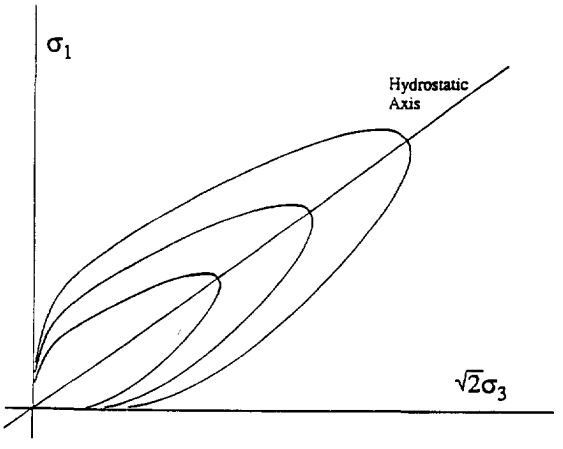

Fig. 1. Plastic potential surfaces shown in triaxial plane.

plastic strain increment under triaxial compression conditions ($\sigma_2 = \sigma_3$) into eqn (15) produces the following equation:

$$\xi_y = \frac{1}{\mu}\xi_x - \psi_2, \tag{16}$$

where

$$\xi_x = \frac{1}{1+\nu_p}\left\{\frac{I_1^3}{I_2^2}(\sigma_1+\sigma_3+2\nu_p\sigma_3)+\psi_1\frac{I_1^4}{I_3^2}(\sigma_1\sigma_3+\nu_p\sigma_3^2)\right\}-3\psi_1\frac{I_1^3}{I_3}+2\frac{I_1^2}{I_2} \tag{17}$$

and

$$\xi_y = \psi_1\frac{I_1^3}{I_3}-\frac{I_1^2}{I_2}. \tag{18}$$

Thus, $1/\mu$ and $-\psi_2$ in eqn (16) can be determined by linear regression between ξ_x and ξ_y calculated from several data points.

2.4. *Yield criterion and work-hardening/softening law*

The yield surfaces are intimately associated with, and derived from, surfaces of constant plastic work, as explained by Lade and Kim (1988a). The isotropic yield function is expressed as follows:

$$f_p = f'_p(\sigma) - f''_p(W_p) = 0, \tag{19}$$

in which

$$f'_p = \left[\psi_1\frac{I_1^3}{I_3}-\frac{I_1^2}{I_2}\right]\left[\frac{I_1}{p_a}\right]^h \cdot e^q, \tag{20}$$

where h is constant and q varies from zero at the hydrostatic axis to unity at the failure surface.

For *hardening*:

$$f''_p = \left[\frac{1}{D}\right]^{1/\rho}\left[\frac{W_p}{p_a}\right]^{1/\rho}, \tag{21}$$

where D and ρ are defined later. The expressions for I_1, I_2, and I_3 in eqn (20) are given in eqns (4), (11), and (7), respectively. The parameter ψ_1 acts as a weighting factor between the triangular shape (from the I_3 term) and the circular shape (from the I_2 term), as in the expression for the plastic potential [eqn (10)]. The constant parameter h is determined on the basis that the plastic work is constant along a yield surface. Thus, for two stress points, A on the hydrostatic axis and B on the failure surface, the following expression is obtained for h:

$$h = \ln\frac{\left[\psi_1\frac{I_{1B}^3}{I_{3B}}-\frac{I_{1B}}{I_{2B}}\right]e}{27\psi_1+3}\Bigg/\ln\frac{I_{1A}}{I_{1B}}, \tag{22}$$

in which e is the base of natural logarithms.

The value of q varies with stress level S, defined as

$$S = f_n/\eta_1 = \frac{1}{\eta_1}(I_1^3/I_3 - 27)\left[\frac{I_1}{p_a}\right]^m, \tag{23}$$

in which f_n is the left-hand side of eqn (6), and η_1 is the value of f_n at failure. The stress level S varies from zero at the hydrostatic axis to unity at the failure surface.

The value of q can now be determined from the test data according to

$$q = \ln \frac{\left[\frac{W_p}{Dp_a}\right]^{1/\rho}}{\left[\psi_1 \frac{I_1^3}{I_3} - \frac{I_1^2}{I_2}\right]\left[\frac{I_1}{p_a}\right]^h}, \tag{24}$$

and the variation of q with S is expressed as

$$q = \frac{\alpha S}{1-(1-\alpha)S}, \tag{25}$$

in which α is constant.

In eqn (21), the values of ρ and D are constants for a given material. Thus, f_p'' varies with the plastic work only. The values of ρ and D are given by:

$$\rho = p/h \tag{26}$$

and

$$D = \frac{C}{(27\psi_1 + 3)^\rho}, \tag{27}$$

in which C and p are used to model the plastic work during isotropic compression:

$$W_p = Cp_a\left(\frac{I_1}{p_a}\right)^p. \tag{28}$$

The yield surfaces are shaped as asymmetric tear-drops with smoothly rounded triangular cross-sections and traces in the triaxial plane as shown in Fig. 2. As the plastic work increases, the isotropic yield surface inflates until the current stress point reaches the

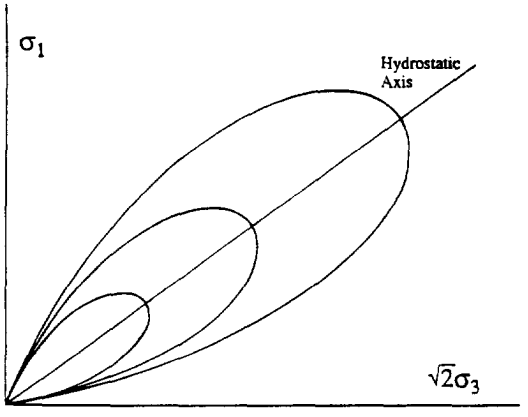

Fig. 2. Yield surfaces shown in triaxial plane.

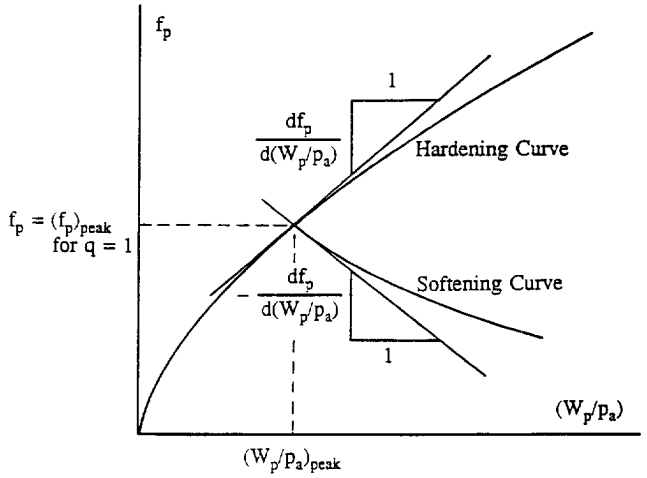

Fig. 3. Modeling of work hardening and softening.

failure surface. The relationship between f_p and W_p is described by a monotonically increasing function whose gradient decreases with increasing plastic work, as shown in Fig. 3.

For *softening* the yield surface deflates isotropically according to an exponential decay function:

$$f_p'' = A\,e^{-B\cdot(W_p/p_a)}, \tag{29}$$

in which A and B are positive constants to be determined on the basis of the gradient of the hardening curve at the point of peak failure, as indicated in Fig. 3.

Using the expression for the plastic potential in eqn (10), the relationship between plastic work increment and the scalar factor of proportionality $d\lambda_p$ in eqn (9) may be expressed as

$$d\lambda_p = \frac{dW_p}{\mu g_p}, \tag{30}$$

in which the increment of plastic work can be determined by differentiation of the hardening and softening equations. For *hardening*, eqn (21) yields:

$$dW_p = Dp_a\rho f_p^{-1}\,df_p \tag{31}$$

and for *softening* eqn (29) produces

$$dW_p = -\left[\frac{1}{B}\right]p_a f_p^{-1}\,df_p, \tag{32}$$

in which df_p is negative during softening.

Combining eqns (31) and (32) with eqn (30) and substituting this and eqns (13a–f) into eqn (9) produces the expression for the incremental plastic strain increments.

2.5. *Materials with effective cohesion*

As explained in connection with the failure criterion, it is possible to include the effective cohesion and the tension that can be sustained by concrete and rock. This is done by translating the principal stress space along the hydrostatic axis, i.e. by adding a constant stress to the normal stress, as in eqn (8), before substitution into the failure criterion in eqn (6).

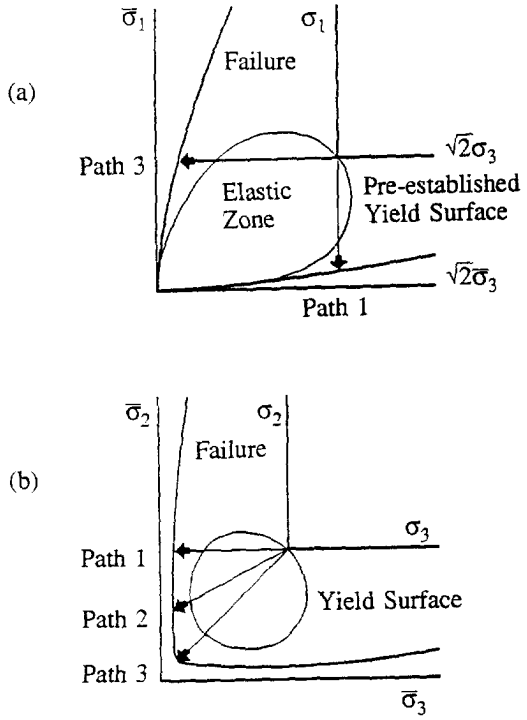

Fig. 4. Biaxial stress paths for concrete employed by Kupfer *et al.* (1969) and assumed initial yield surface in (a) triaxial plane and (b) biaxial plane.

A similar technique has been shown to work for the elastic modulus variation (Lade and Nelson, 1987), the plastic potential (Kim and Lade, 1988), the yield criterion, and the work-hardening/softening law (Lade and Kim, 1988a). Inconsistencies in the plastic behavior of materials with effective cohesion are overcome by assuming that there exists an initial yield surface which goes through the origin of the real stress space, as shown in Fig. 4. This implies that only elastic strains occur during the major portions of tension-type tests in which the main parts of the stress paths are located inside the yield surface. Thus, the stresses applied along the stress paths indicated in Fig. 4 do not produce plastic strains until they are close to failure. The existence of an initial yield surface appears to simulate experimental observations with good accuracy.

The technique of performing all calculations in the translated stress space provides a convenient tool for mathematical treatment of cohesive materials. Following all the necessary calculations, the stresses are again modified to hold conventional physical meaning. For cohesionless materials for which 'a' is zero, the calculations are performed in the original stress space.

3. PARAMETER VALUES

The results of isotropic compression tests and isotropically consolidated drained and undrained triaxial compression tests were available for loose and dense Sacramento River sand with initial void ratios of 0.87 and 0.61, corresponding to relative densities of 38% and 100%, respectively (Lee, 1965; Lee and Seed, 1967; Seed and Lee, 1967). the necessary soil parameters were derived from the isotropic compression and drained triaxial compression tests, and the values of these parameters are given in Table 1. The results of the undrained triaxial compression tests are used for comparison with the predictions of the single hardening stress–strain model below.

The experimental data for plain concrete tested in the biaxial plane by Kupfer *et al.* (1969) were used to demonstrate the capabilities of the model for materials with effective cohesion such as rock and concrete. The required number of parameters for a material with effective cohesion is 12. For cohesionless materials, the value of $a = 0$. All other parameters

Table 1. Parameter values for loose and dense Sacramento River sand and for plain concrete

Parameter		Sacramento River sand†		Plain concrete‡
Relative density, D_r (%)		38	100	—
Void ratio, e		0.87	0.61	—
Elastic moduli	ν	0.2	0.2	0.18
	M	500	900	361 800
	λ	0.28	0.28	0
Failure criterion	a	0	0	28.5
	m	0.093	0.23	1.113
	η_1	28	80	159 800
Plastic potential	ψ_2	−3.72	−3.09	−2.92
	μ	2.36	2.00	5.06
Hardening function	C	0.127×10^{-3}	0.396×10^{-4}	0.712×10^{-12}
	p	1.65	1.82	3.80
Yield function	h	0.534	0.765	1.990
	α	0.794	0.229	0.75

† Data from Lee (1965) and from Lee and Seed (1967).
‡ Data from Kupfer *et al.* (1969).

have values different from zero for most frictional materials. The parameter values pertaining to the plain concrete tested by Kupfer *et al.* (1969) are given in Table 1. The elastic parameters were determined from the tension–tension tests in which only elastic deformations occur until the pre-existing yield surface is reached. However, these data were not sufficient to determine the elastic modulus variation with stress state, and Young's modulus was therefore taken to be constant for the purpose of predicting the biaxial tests. All other parameter values were determined from the compression–compression data for the plain concrete.

4. PREDICTIONS FOR UNDRAINED TESTS ON SAND

The prediction of pore pressures in undrained tests on saturated specimens is based on the condition that no volume change occurs in the soil for any load increment:

$$\Delta\varepsilon_v^e + \Delta\varepsilon_v^p = 0, \tag{33}$$

where $\Delta\varepsilon_v^e$ and $\Delta\varepsilon_v^p$ are the volumetric strain components corresponding to the two types of strain occurring in soil. The calculation of pore pressures was performed by specifying the cell pressure and discrete values of effective stress ratio, σ_1'/σ_3', or stress difference, $(\sigma_1-\sigma_3)$. The effective confining pressure producing volumetric strains that would satisfy eqn (33) within specified limits was found by iteration. After having satisfied eqn (33), the pore pressure was calculated as the difference between the cell pressure and the effective confining pressure found by iteration. It should be noted that calculation of pore pressures using the restraint in eqn (33) is based on the fact that a balance can be found between the compressive and the expansive volumetric strain components such that their sum is zero for each value of σ_1'/σ_3', or $(\sigma_1-\sigma_3)$.

Examples of measured and predicted pore pressure and stress–strain behavior are shown in Figs 5 and 6 for tests on loose and dense Sacramento River sand with initial consolidation pressures of 1070 and 1030 kPa, respectively. The points on these figures represent the measured soil behavior and the solid lines represent predictions from the theory.

Back pressures were not used in the undrained tests. This was taken into account in the calculations using the single hardening model. It was observed that the pore water cavitated at about −0.9 atmospheres (approximately −90 kPa) in tests performed with low initial effective confining pressures (Lee, 1965). The fact that cavitation occurred at −0.9 atmospheres was included in the computer program used for the predictions.

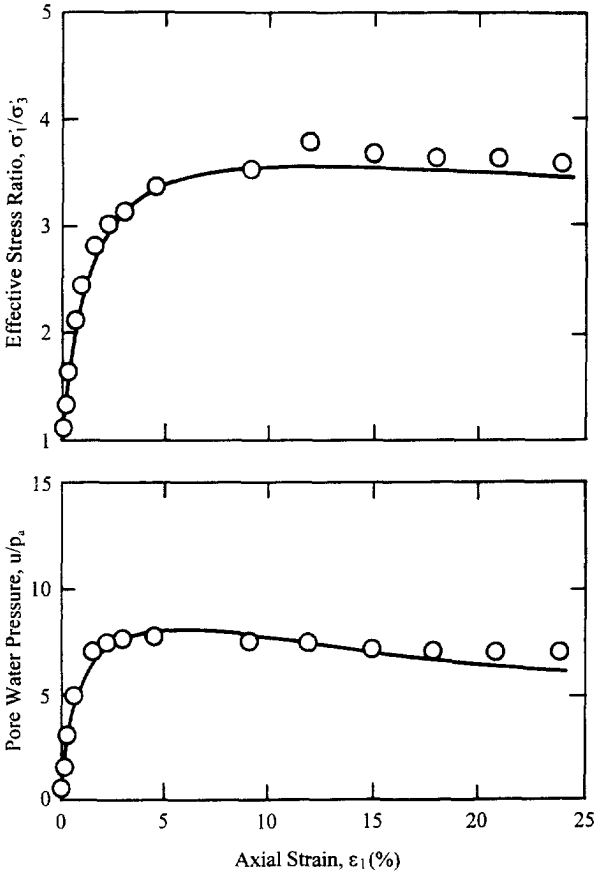

Fig. 5. Comparison of predicted and observed behavior of loose Sacramento River sand tested by Seed and Lee (1967) in undrained triaxial compression tests initially consolidated at 1070 kPa.

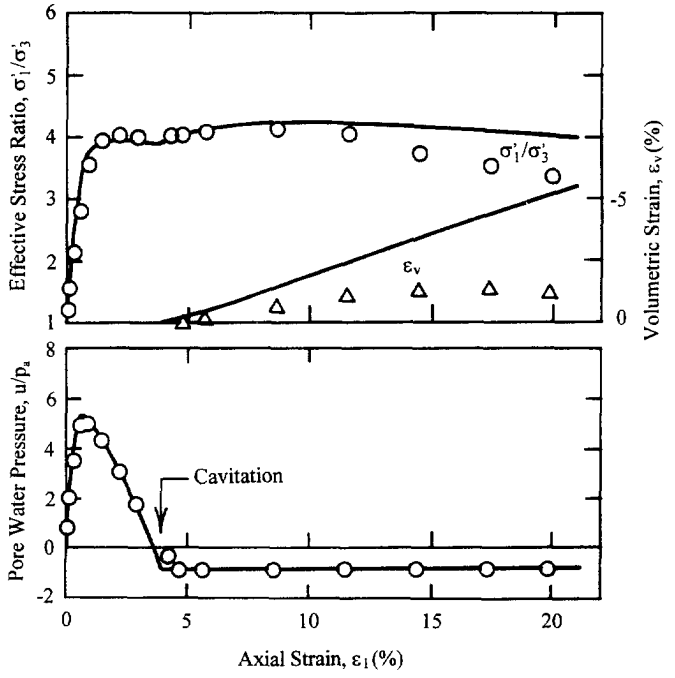

Fig. 6. Comparison of predicted and observed behavior of dense Sacramento River sand tested by Seed and Lee (1967) in undrained triaxial compression tests initially consolidated at 1030 kPa.

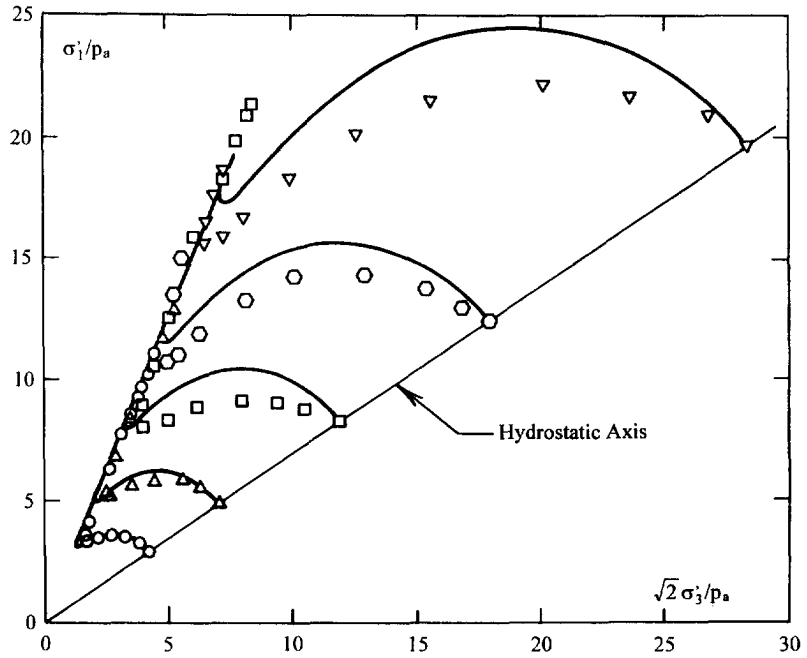

Fig. 7. Comparison of predicted and observed effective stress paths in undrained triaxial compression tests on loose Sacramento River sand performed by Seed and Lee (1967).

Figure 5 shows that the stress–strain and pore pressure predictions compare favorably with the behavior measured in the undrained test on loose Sacramento River sand. The results of the undrained tests on dense Sacramento River sand are also predicted with good accuracy, as shown in Fig. 6. Cavitation of the pore water occurred in this test and the consequent expansion of the specimen is reasonably well predicted by the model.

The effective stress paths obtained from predictions are compared with the measured stress paths for several tests on loose and dense Sacramento River sand on the triaxial planes in Figs 7 and 8. The effective stress paths are very sensitive to differences between predicted and measured pore pressures, especially at small strains. The diagrams in Figs 7 and 8 show that some differences between measured and predicted behavior are present, but the stress paths predicted for the undrained tests generally compare favorably with those observed. In particular, the model is clearly capable of differentiation between the undrained behavior of loose and dense sand. Thus, loose sand consolidated to sufficiently high pressures before undrained shearing follows effective stress paths along which all stresses decrease while plastic strains are produced. This behavior is indicated by the effective stress paths in Fig. 7, and it corresponds to conditions for which loose sand can become unstable inside the failure surface. The mechanics of instability and subsequent liquefaction has been explained by Lade (1992). This has served as a background for explanations of submarine flow slides (Lade, 1992, 1993b), instability of tailings slopes (Lade, 1994), and liquefaction of loose sand (Lade, 1994a). The possibility that such events may occur can be predicted from analyses in which a constitutive model such as the one presented here is employed.

5. PREDICTIONS FOR PLAIN CONCRETE

Figure 9 shows predictions for the suite of nine biaxial tests performed by Kupfer *et al.* (1969). Results were available in each of the three regions comprising compression–compression, compression–tension, and tension–tension. The direction of the stress path in the biaxial plane is shown for each test.

As explained previously, the stress components in all stress functions correspond to the translated stresses given in eqn (8). The translation of stresses is performed at the initial input state and the reverse translation is performed before the stresses are obtained for

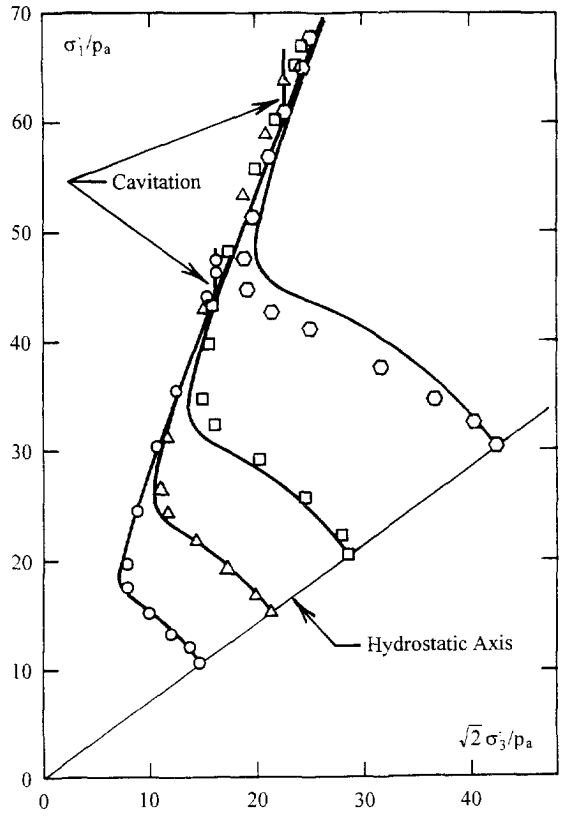

Fig. 8. Comparison of predicted and observed effective stress paths in undrained triaxial compression tests on dense Sacramento River sand performed by Seed and Lee (1967).

plotting. The nine diagrams show accurate predictions of the stress–strain curves. Although the material parameters were determined from the compression–compression data, the model predicts the compression–tension tests in a consistent manner. The effects of the intermediate principal stress on the stress–strain curves are captured well in the model predictions. The tension–tension tests primarily involve elastic deformations. Thus, it is expected that good agreement between prediction and experiment is obtained, because the elastic parameters were determined from the results of these tests. Near failure, a sudden increase in plastic strains is predicted as a result of the presence of the pre-existing yield surface as shown in Fig. 4. The results appear to verify the concept of a pre-existing yield surface in the tensile stress region.

6. CONCLUSIONS

The behavior of frictional materials is such that a unified approach is possible in describing their failure surfaces as well as their stress–strain relationship. A combination of elasticity theory and plasticity theory provides a reasonable and consistent description of this behavior when appropriate mathematical functions are used in the framework given by these theories. In addition to Hooke's law, the components in this framework are the failure criterion, the flow rule, the yield criterion, and the work-hardening/softening law. Analyses of experimental data indicate that the shapes of the failure, yield, and plastic potential surfaces obtained from different types of frictional material each have similar characteristics and may be modeled by similar mathematical functions. These functions are all expressible in terms of the three invariants of the stress tensor.

The model requires twelve parameters for materials with effective cohesion such as concrete, and eleven parameter values for cohesionless materials. These parameters can be determined from simple laboratory tests such as isotropic compression and triaxial compression tests or from any other set of tests in which all stresses and strains are measured.

The capabilities of the single hardening model are demonstrated by predictions of two widely different behavior patterns for frictional materials. Predictions of stress–strain relationships, pore pressure variation, expansion after cavitation, and effective stress paths compare favorably with experimental results for loose and dense Sacramento River sand. Conditions resulting in instability and subsequent liquefaction can be predicted using the single hardening model presented here.

The results of biaxial tests on plain concrete presented in the literature served as a basis for evaluating the capabilities of the model for materials with effective cohesion. In particular, comparisons of measured and predicted behavior were shown for nine tests,

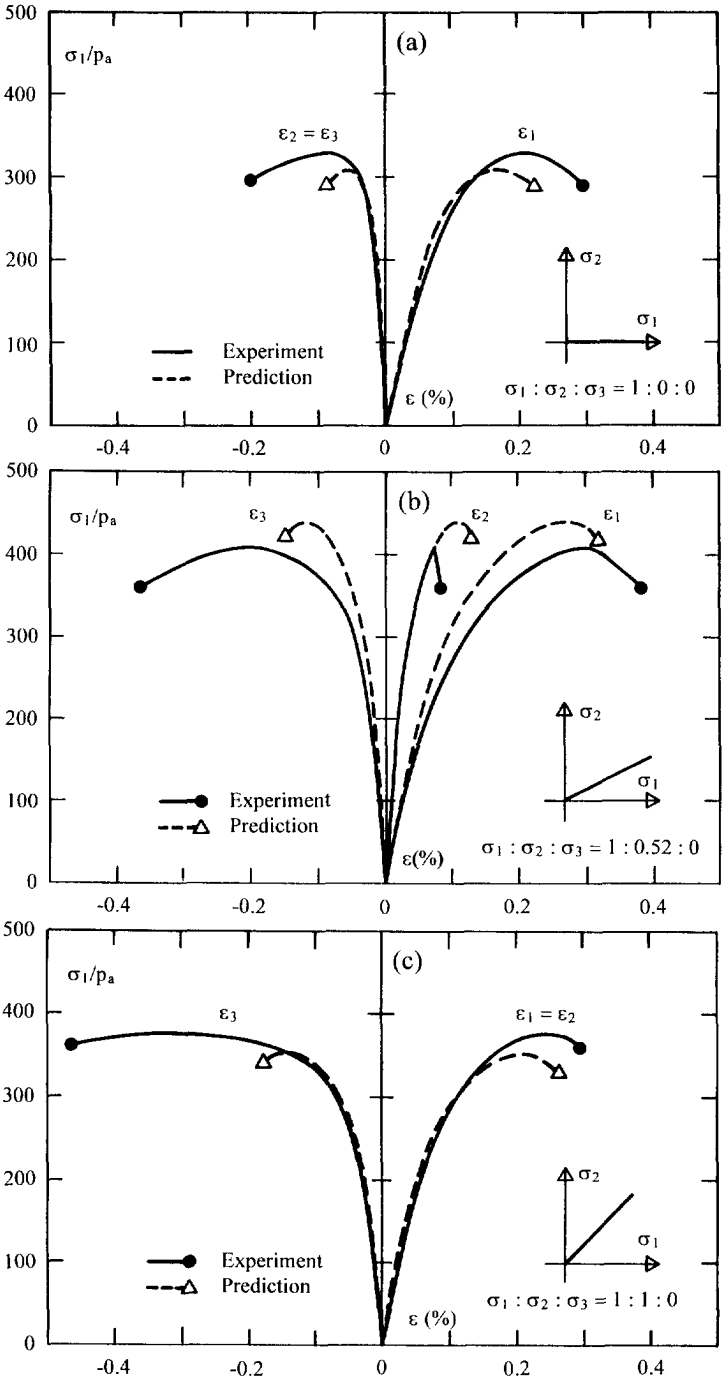

Fig. 9(a–i). Comparison of predicted and observed stress–strain relationships for biaxial tests on plain concrete tested by Kupfer *et al.* (1969). Stress paths are shown on inserts.

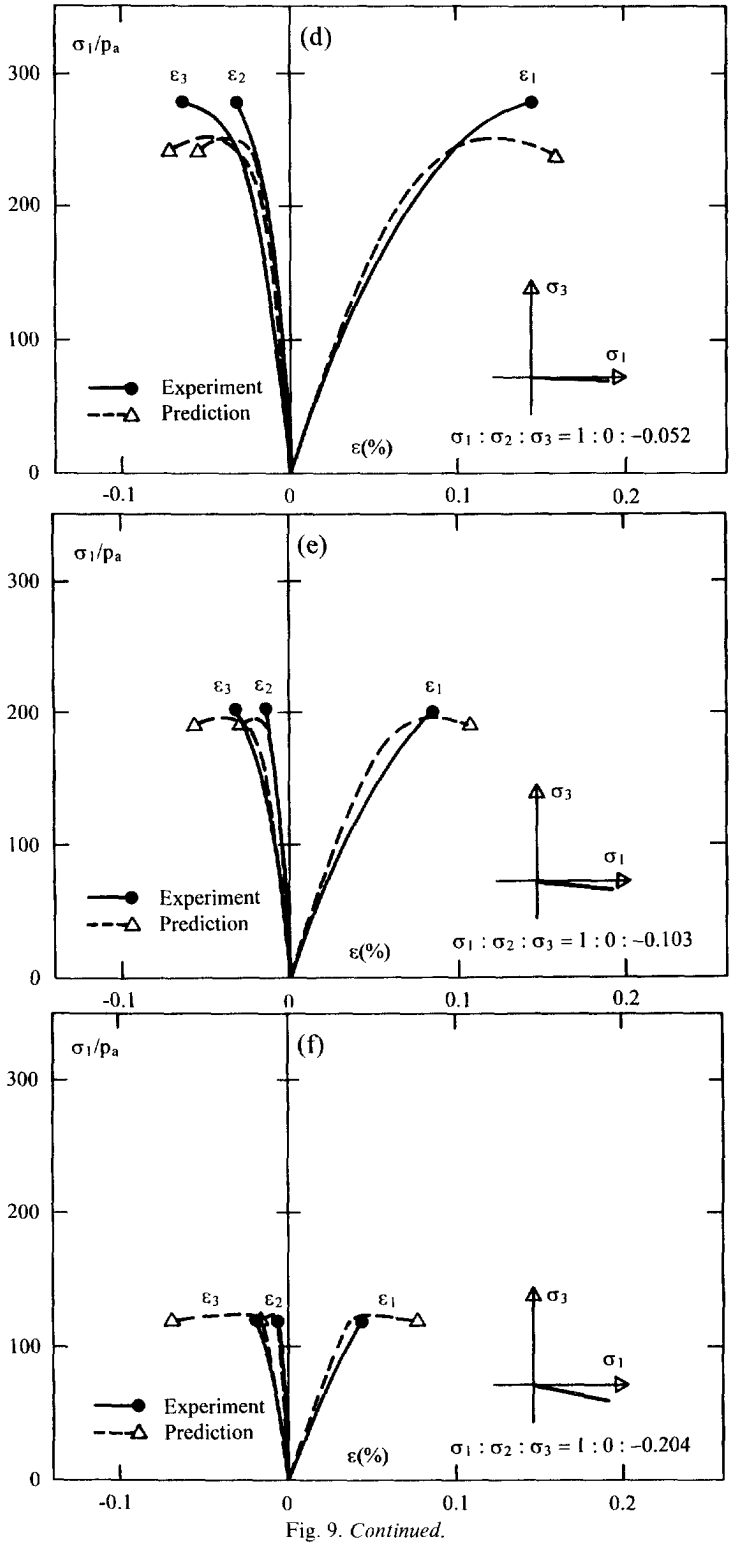

Fig. 9. *Continued.*

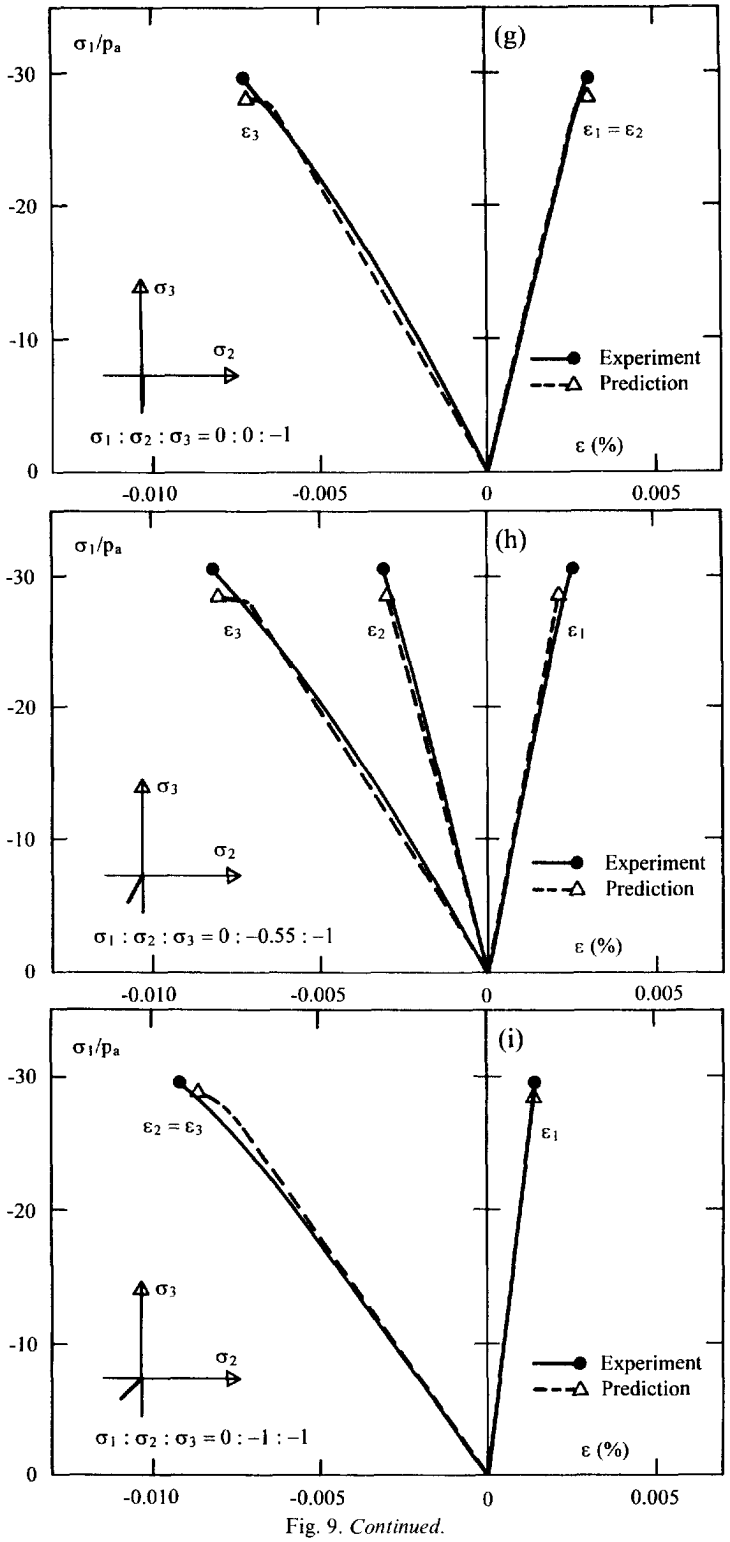

Fig. 9. *Continued.*

three in each of the regions of compression–compression, compression–tension, and tension–tension. Overall acceptable and accurate predictions were produced for the plain concrete.

Acknowledgment—This study was supported by the National Science Foundation under Grant No. CEE 8211159. Grateful appreciation is expressed for this support.

REFERENCES

Kim, M. K. and Lade, P. V. (1984). Modelling rock strength in three dimensions. *Int. J. Rock Mech. Min. Sci. & Geomech. Abstr.* **21,** 21–33.

Kim, M. K. and Lade, P. V. (1988). Single hardening constitutive model for frictional materials, I. Plastic potential function. *Computers & Geotech.* **5,** 307–324.

Kupfer, H., Hilsdorf, H. K. and Rusch, H. (1969). Behavior of concrete under biaxial stresses. *J. Am. Concr. Inst.* **66,** 656–666.

Lade, P. V. (1977). Elasto-plastic stress–strain theory for cohesionless soil with curved yield surfaces. *Int. J. Solids Structures* **13,** 1019–1035.

Lade, P. V. (1982). Three-parameter failure criterion for concrete. *ASCE J. Engng Mech. Div.* **108,** 850–863.

Lade, P. V. (1984). Failure criterion for frictional materials. In *Mechanics of Engineering Materials* (Edited by C. S. Desai and R. H. Gallagher), pp. 385–402. Wiley, New York.

Lade, P. V. (1992). Static instability and liquefaction of loose fine sandy slopes. *ASCE J. Geotech. Engng* **118,** 51–71.

Lade, P. V. (1993a). Rock strength criteria: the theories and the evidence. Ch. 11, Vol. I In *Comprehensive Rock Engineering, Principles, Practice and Projects* (Edited by J. A. Hudson *et al.*) Vol. I, ch. 11, pp. 255–284. Pergamon Press, Oxford.

Lade, P. V. (1993b). Initiation of static instability in the submarine Nerlerk Berm. *Can. Geotech. J.* **30,** 895–904.

Lade, P. V. (1994a). Instability and liquefaction of granular materials. *Computers & Geotech.* **16,** 123–151.

Lade, P. V. (1994b). Instability analysis for tailings slopes. In *Proc. 13th Int. Conf. Soil Mech. Found. Engng*, pp. 1649–1652. New Delhi, India.

Lade, P. V. and Kim, M. K. (1988a). Single hardening constitutive model for frictional materials, II. Yield criterion and plastic work contours. *Computers & Geotech.* **6,** 13–29.

Lade, P. V. and Kim, M. K. (1988b). Single hardening constitutive model for frictional materials, III. Comparisons with experimental data. *Computers & Geotech.* **6,** 30–47.

Lade, P. V. and Nelson, R. B. (1987). Modelling the elastic behavior of granular materials. *Int. J. Num. Anal. Meth. Geomech.* **11,** 521–542.

Lee, K. L. (1965). Triaxial compressive strength of saturated sand under seismic loading conditions. PhD thesis, Univ. of California, Berkeley.

Lee, K. L. and Seed, H. B. (1967). Drained strength characteristics of sands. *ASCE J. Soil Mech. Found. Div.* **93 SM6,** 117–141.

Seed, H. B. and Lee, K. L. (1967). Undrained strength characteristics of sands. *ASCE J. Soil Mech. Found. Div.* **93** (SM6), 333–360.